# Enhanced grain growth and dielectric properties in aerosol deposited BaTiO$_3$

Marcus Bentzen [a,*], Juliana Maier [b], Udo Eckstein [b], Jianying He [c], Anja Henss [d], Neamul Khansur [b], Julia Glaum [a]

[a] *Department of Materials Science and Engineering, Norwegian University of Science and Technology, Sem Sælands vei 12, 7034 Trondheim, Norway*
[b] *Department of Materials Science and Engineering, Friedrich-Alexander-Universität Erlangen-Nürnberg (FAU), Martensstraße 5, 91058 Erlangen, Germany*
[c] *Department of Structural Engineering, Norwegian University of Science and Technology, Richard Birkelands vei 1A, 7034 Trondheim, Norway*
[d] *Justus-Liebig University, Heinrich-Buff-Ring 17, 35392 Gießen, Germany*

## ARTICLE INFO

## ABSTRACT

Piezoelectric ceramics are envisioned as cell stimulating materials for *in-vivo*, load-bearing applications. To compensate for their brittle nature developing ceramic films on medically accredited metals is a promising approach. However, high temperature consolidation is often required to achieve highly dense ceramics with suitable functional properties, which can compromise the metal substrate integrity. With aerosol deposition highly dense thick films can be produced at room temperature. Still, an annealing step is required to enhance the functional properties of piezoelectric ceramics. Thermal annealing of dense, aerosol deposited BaTiO$_3$ thick films on 304SUS stainless steel gave a clear enhancement of the dielectric properties. An increase in saturation polarization and the adoption of ferroelectric hysteresis at 750 °C coincided with a significant reduction in mechanical properties. The simultaneous appearance of grain growth and diffusion of chromium from the substrate at 750 °C suggests that chromium acts as a sintering aid.

## 1. Introduction

Piezoelectrics are a class of functional materials possessing the unique emergent property of generating electrical surface charge upon application of mechanical stress, and *vice versa*. This has made piezoelectrics one of the most technologically important material classes of modern society, with applications ranging from ultrasound transducers for medical imaging to low orbit satellite mounted optics [1,2]. The advent of micro and nano-electronics has created considerable interest in combining piezoelectric ceramic films with substrate materials such as metals, polymers and glass. Combination of these different materials is in general to make systems where the components complement each other's properties, such as functional ceramic films with mechanically strong metals. One such new application is the use of piezoelectric ceramic thick or thin films as bone growth enhancers on the surface of orthopedic metal implants.

This combination of materials utilizes the electrical activity of the piezoelectric ceramics with the strength and ductility of the load-bearing underlying metal implants [3–5]. However, for such an implant to work, the film needs to be dense and strongly adhered to the implant to prevent it from coming off or disintegrating *in-vivo* while retaining the functional properties of the film. This has provided a considerable challenge when exploring suitable processing routes as one of the principal ways for ceramic film deposition to achieve adherence and densification is by the application of high temperatures to fuse the film with the substrate and consolidate it [5]. In particular, densification and adherence of ceramics to substrates can require temperatures above 1000 °C [6,7] which could drastically alter the chemistry and stability of the substrate. As such, room temperature processing is an area of intense research, with one possible candidate being Aerosol Deposition (AD).

Although comparatively novel in the west, AD research has been dominated by South Korea and Japan since the 1990′s following its invention by Ichiki et al. [8] and subsequent pioneering work by Akedo et al. [9–12]. So far, a sizable amount of the research has been focused on the development of microelectromechanical systems (MEMS) for use as microactuators and energy harvesting [6]. However the process' operating principles suggests that it could be useful for the fabrication of functional films for orthopedic implants as well. The method involves

accelerating ceramic particles to velocities of 100–600 m/s through a specialized nozzle onto a wide range of substrate materials and geometries at room-temperature [9]. Once accelerated, the high kinetic energy of the particles is enough to fracture them upon impact with the substrate and plastically deform them, leading to a dense film with successive impacts. The accepted mechanism for this process is typically referred to as room temperature impact consolidation (RTIC) and is excellently summarized along with the AD process itself in a review by Hanft et al. [6]. By virtue of the RTIC mechanism, as-sprayed AD films show a large degree of microstructural homogeneity regardless of film and substrate material. Generally speaking, an AD film exhibits few defects, excellent contact and adhesion with the substrate, low porosity, nano-scale grains, high dielectric breakdown strength, large residual strain and densities higher than 96% [13]. Based on this, AD is a promising candidate for integrating ceramics with possibly temperature sensitive substrates, yet there are some drawbacks.

Although there are several studies reporting successful room-temperature deposition of ceramics such as $Al_2O_3$ [14,15], materials possessing piezoelectric or ferroelectric character have been proven more difficult to process. Specifically, many piezoelectrics show reduced dielectric properties when grain or crystallite sizes enter into the nano-scale [16,17]. Additionally, as piezoelectricity is strain dependent, the presence of residual strain introduced by the RTIC deposition mechanism in AD films can further limit the electromechanical functionality of the material [18]. In response to this, post-processing heat-treatments are a common way to increase crystallite sizes and release some of the residual strain present in the as-processed AD films [19–21].

The issue is that these heat-treatments can sometimes exceed 1000 °C [22,23] depending on the film material, effectively negating the room-temperature advantage of AD. Additionally, such post-processing adds another layer of complexity to the method and necessitates optimization for specific material combinations.

In this study, optimization of post-processing heat-treatments was investigated for aerosol deposited $BaTiO_3$ thick films on a cost-effective and widely used medical grade stainless steel substrate. Dielectric testing shows greatly enhanced dielectric properties with increasing heat-treatment temperature. Accompanying characterization of crystal structure, microstructural features, and mechanical properties reveal a correlation between enhanced dielectric properties and mechanical stability, grain growth and residual internal stress within the samples. Lastly, observed microstructural changes in this study suggests that diffusion of chromium metal to the film surface from the substrate enhances grain growth.

## 2. Material and methods

$BaTiO_3$ ceramic films with a 11–12 µm thickness were deposited onto 304SUS stainless steel substrates (INOX-COLOR GmbH & Co KG.) using BT powders produced by the conventional solid-state reaction method. Raw powders of $TiO_2$ (Alfa Aesar, 99.6% purity) and $BaCO_3$ (Alfa Aesar, 99.8% purity) were stoichiometrically weighed, mixed and homogenized for 24 h. Mixed powders were then calcined at 1100 °C for 6 h. Calcined powders were wet-milled in 96% EtOH for 15 h using 5 mm yttria-stabilized zirconia milling balls in a rolling mill at 70 rpm. A median particle size of $d_{50} \approx 1.2$ µm was achieved and deemed appropriate for the aerosol deposition setup being used. The powders were then vacuum dried at 180 °C for at least 24 h before deposition.

Finished powders were then deposited onto 1 cm x 1 cm x 1 mm mirror polished (2 P/no.7 and 2 P/no.8) 304SUS stainless steel substrates using aerosol deposition. The deposition process utilized a rectangular nozzle with an orifice size measuring 0.5 mm x 10 mm to accelerate $N_2$ carrier gas at a rate of 4 L/min. The distance between the nozzle and substrate was kept constant at 7 mm.

As-sprayed samples were quartered into 0.25 cm $\times$ 0.25 cm x1mm pieces using a Wells 3500 Series Diamond Wire Saw with a 0.3 mm thick

diamond coated wire. Cut samples were heat-treated in air using a Kanthal Super box furnace with holding temperatures being 400 °C, 550 °C, 650 °C, and 750 °C for 2 h with a heating/cooling rate of 3 °C/min.

Phase and chemical composition of the films was ascertained using X-ray diffraction (XRD), Energy Dispersive X-Ray Spectroscopy (EDS), and Time-of-Flight Secondary Ion Mass Spectrometry (ToF- SIMS). XRD measurements were conducted using a Bruker D8 A25 DaVinci X-ray Diffractometer with Bragg-Bretano geometry and *CuK*α 1.54 Å radiation (Bruker Corp., Massachusetts, USA). DIFFRAC.EVA and DIFFRAC. TOPAS software (Bruker Corp., Massachusetts, USA) was used to assess the diffractograms. TOPAS analysis took into account instrument contributions and the exclusion of W contamination wavelengths by using a recent emission profile made using an $LaB6$ standard. EDS was used to observe the chemical make-up of the substrate-film interface using a Quantax EDS system (Bruker Corp., Massachusetts, USA) mounted to a Zeiss Supra 55VP FESEM (Carl Zeiss AG. Oberkochen. Germany), with the latter instrument also being used so produce the scanning electron microscope images presented. Analysis of the EDS data was performed in the TEAM™EDS Analysis System software.

The ToF-SIMS measurements were conducted using a M6 hybrid SIMS instrument (IONTOF GmbH, Muünster. Germany), which is equipped with a 30 kV Bi cluster primary ion gun for sputtering and analysis and a 20 kV gas cluster ion source (GCIS), as well as a dual-source column with $O_2^+$ and $Cs^+$, low-energy guns for depth profiling. Depth profiles were measured in spectrometry mode (bunched). The spectrometry mode provides high signal intensity and high mass resolution 40,000 cts/s, FWHM $m/\Delta m = 8000$ at $m/z = 47.94$ ($Ti^+$)). Surface measurements were recorded in spectrometry mode (100 $\times$100 µm$^2$) keeping the ion dose density below $10^{12}$ ions/cm$^{-2}$. Depth profiles in spectrometry mode were acquired with $O_2^+$ ions (2 keV, 150 $\times$150 µm$^2$) as sputter species and $Bi^+$ (1.2 pA, 75 $\times$75 µm$^2$) as primary ion mode. All measurements were carried out in positive. Data evaluation was carried out with the software SurfaceLab 7.2 (IONTOF GmbH).

Polarization-electric field loops were collected in a TF Analyser 2000 (aixACCT (aixPES). Aachen, Germany) utilizing painted-on silver electrodes (Auromal®- 50 L Silberleitlack. Ami Doduco GmbH) and insulating silicon oil (Wacker®- AP 100 Silicone Fluid). Measurements were carried out using a frequency of 100 Hz.

Reduced modulus $E_r$ and hardness $H$ of the films were measured by nano-indentation (NI) using a Hysitron TI 950 TriboIndenter. The measurement was made by making a series of 7–9 indentation (sample dependent) across a 60 µm x 60 µm area. The indentation followed a linear load/deload function which applied up tp 10 mN of mechanical force with a maximal indenter displacement of 5 µm. The instrument can detect changes in force and displacement down to 0.4 nN and 0.01 nm respectively.

## 3. Results

### 3.1. Crystal structure

XRD measurements performed on the samples revealed that the heat-treatment had little effect on the chemical makeup of the BT films. As seen in Fig. 1a) the samples show no new peaks compared to their as-sprayed state with the exception of five new minor peaks in samples heat-treated at 750 °C. These peaks correspond to $BaCrO_4$, while the major phase was identified as $BaTiO_3$. The crystal structure of the $BaTiO_3$ major phase is obscured by strong peak broadening, giving the diffractogram a psuedo-cubic appearance. Additionally the effect of the heat-treatment can be seen on the shape and position of the $BaTiO_3$ peaks (Fig. 1b)). With increasing temperature the peak broadening is significantly reduced and peak positions were shifted towards higher angles. The largest peak shifts from the as-sprayed starting position were observed for the 400 °C and 550 °C treated samples. Samples heated to 650 °C and 750 °C were also shifted to higher angles albeit to a lesser degree than for low temperatures. The changes to the XRD
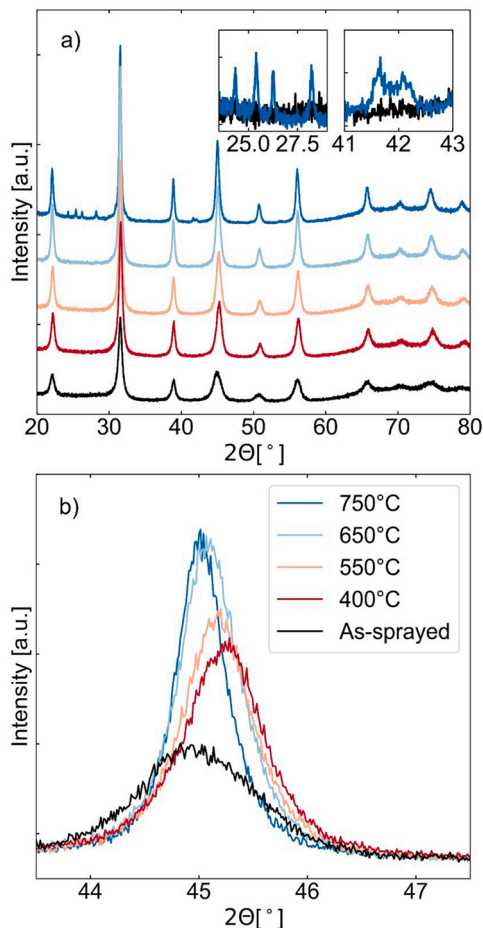
**Fig. 1.** a) XRD diffractograms for AD BaTiO$_3$ films on stainless steel before and after post-processing heat-treatments. The top right insets show the appearance of characteristic BaCrO$_4$ peaks. b) (200) reflection showing the peak shifts with changing temperature.

diffractograms correspond to an overall doubling of the crystallite sizes calculated in TOPAS from ~ 920 nm (Table 1). The crystallite sizes are reported as LVol-IB (Volume weighted mean Length - Integral Breadth) which uses the Full Width Half Maximum (FWHM) and integral breadth to give volume- weighted mean crystallite sizes with Lorentzian and Gaussian component convolutions.

### 3.2. Microstructure

The samples' microstructure as observed in SEM did not change significantly from the film's as-sprayed state as a function of heat-treatment until the 750 °C condition. The as-sprayed samples show a surface microstructure typical to the aerosol deposition method (Fig. 2a) with nano-sized, powder-like particles compacted into a dense film with elevated ridges surrounding impact craters. Larger particles can be seen scattered across the sample surface. These particles can stem from

**Table 1**
DIFFRAC.TOPAS calculated crystallite sizes for as-sprayed and heat-treated films.

| Sample | LVol-IB (nm) |
|---|---|
| As-Sprayed | 9.4 ± 0.2 |
| 400 °C | 11.8 ± 0.9 |
| 550 °C | 13.1 ± 0.2 |
| 650 °C | 15.5 ± 0.2 |
| 750 °C | 20.3 ± 0.4 |

smaller particles in the initial powder which did not break upon impact, fractured pieces of larger initial particles or agglomerates which broke upon impact.

The SEM image of the as-sprayed film-substrate interface (Fig. 2b) reveals excellent bonding between the film and substrate with no apparent porosity at the interface. The film itself shows slightly lamellar layers which correspond to single passes of the scanning AD particle spray. It is suggested that such layers are formed by the plastic deformation of piled and stacked particles upon successive impacts [24]. Small voids containing loosely agglomerated, improperly fractured particles can be seen throughout the film cross-section (Fig. 2b).

Heat-treatment at 750 °C produced clear grain growth at the surface of the film with grains ranging from ~ 0.3–1.2 μm in size (Fig. 2c). Grain growth was also observed in some samples heat-treated at 650 °C. Additionally, grain growth in the 750 °C treated samples was not uniformly distributed on the surface for all samples, with some having higher degrees of densification towards the sample edge and less towards the center. For most 750 °C treated samples an apparent consolidation of the film with fusing of the lamellar layers, and adoption of a much more uniform appearance was observed (Fig. 2d). Contrary to the surface, growth of individual grains in the interior of the samples cannot be seen. The larger agglomerate-filled voids in the as-sprayed samples have been replaced by evenly distributed, equally sized nanopores. Contact between the film and substrate appears largely unchanged with the absence of voids or defects along the film-substrate interface.

### 3.3. Mechanical properties

Nano-indentation showed a clear change in the mechanical properties of the films after heat-treatment as seen in the force-displacement curves in Fig. 3a-c). The figure shows the penetration of the indentor head into the sample films with increasing applied force. Each curve corresponds to a different point on the sample. The resulting curve is then used to calculate the reduced modulus $E_r$ and hardness $H$. Values for $E_r$ and $H$ are given in Table 2 with errors being determined from multiple measurements at different spots on each sample.

The curves and corresponding calculated values show an initial improvement of mechanical properties for samples treated at 550 °C. Subsequently, a deterioration of properties is observed for higher temperatures along with a spike in the variability of the measurements. This trend is reflected in the force-displacement curves' shape. As-sprayed samples (Fig. 3a) show a small spread in the force displacement curves with generally steep exponential slopes. For samples heat-treated at 550 °C these slopes are steep and linear with all curves being strongly consolidated around the same displacement values, encompassing roughly the same area. Once the temperature is increased to 750 °C a clear change occurs where the curves spread out widely in position and shape. Both steep and shallow curves can be observed as well as shoulders showing sudden large increases in displacement.

### 3.4. Dielectric properties

Dielectric properties of the AD films are shown in Fig. 4 in the form of polarization-electric field loops. As-sprayed samples showed little to no polarization under high fields. Polarization behavior improved for samples heat-treated at 400 °C and 550 °C with large relative increases to saturation and remanent polarization. The 550 °C sample possessed the highest saturation and remanent polarization of all samples with values of ~ 7.5 μC/cm$^2$ and ~ 4.5 μC/cm$^2$, respectively. However, the 550 °C treated sample was quite conductive as seen by the rounded appearance of the polarization-electric field loop falsely indicating that polarization increases even as the electric field is reversed. Once samples were treated at 650 °C, clear ferroelectric hysteresis behavior started to develop, which was further enhanced in the sample heated up to 750 °C along with a reduction in conductivity. Saturation and remanent polarization values of the 750 °C sample were ~ 5.3 μC/cm$^2$ and ~ 2.5 μC/
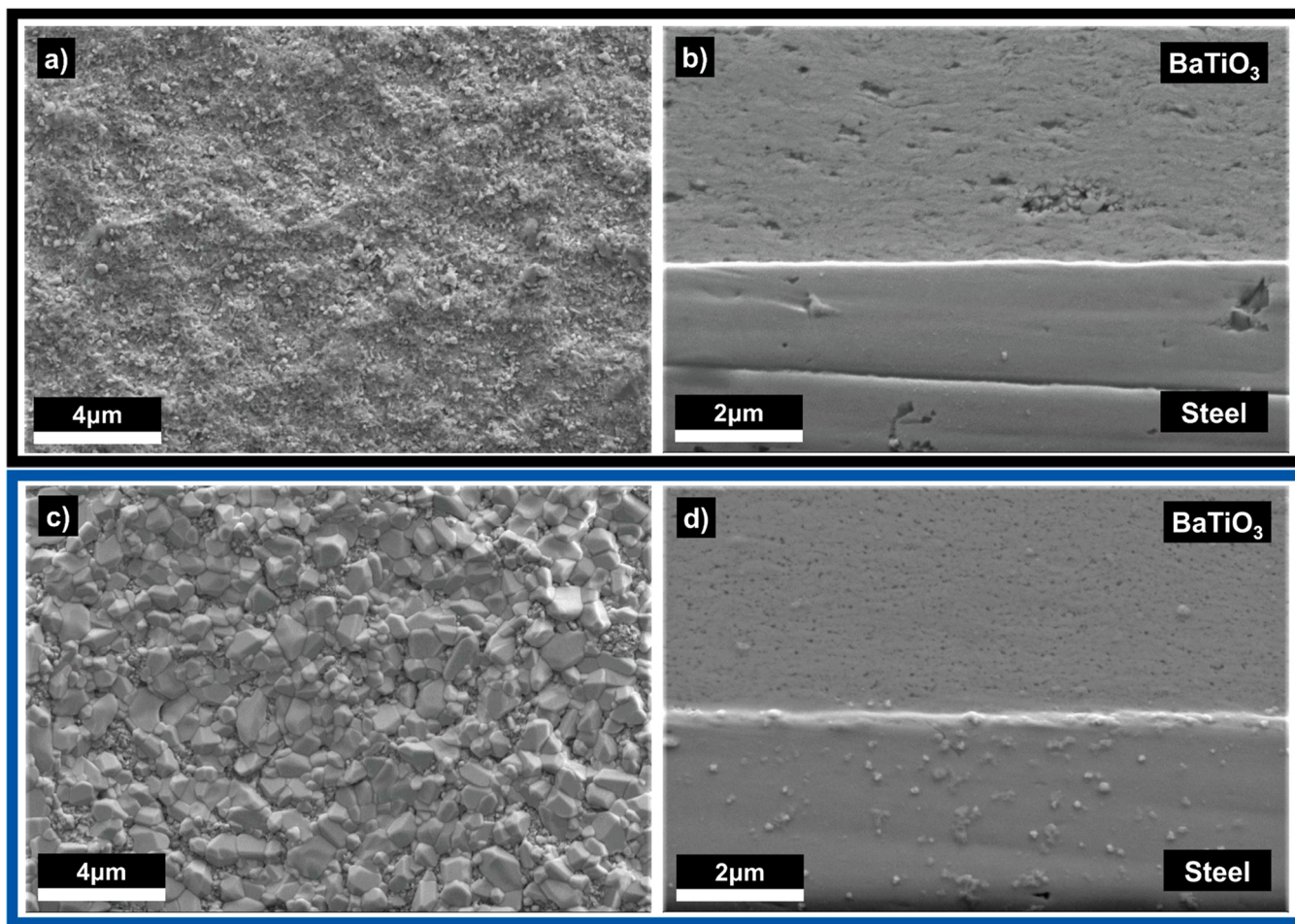
**Fig. 2.** SEM micrographs of: a) As-sprayed surface. b) Film-substrate interface of as-sprayed sample. c) 750 °C treated sample surface. d) 750 °C treated sample film-substrate interface. Cross sections were prepared using a diamond suspension polishing regiment.

cm$^2$, respectively.

### 3.5. Elemental distribution

Fig. 5 shows ToF-SIMS depth profiles on the left and EDS maps on the right for an as-sprayed (Fig. 5a) and a heat-treated (750 °C) sample (Fig. 5b), respectively. The ToF-SIMS depth profile describes the composition from the film surface to a small distance into the substrate, crossing the substrate-film interface. The interface of both samples is characterized by a sudden drop in barium and titanium content, and a rise in the steel alloying elements.

The as-sprayed sample (Fig. 5a) shows frequent drops in barium and titanium intensity within the depth profile and clear voids (*i.e.* black dots) in its accompanying SEM image. However, it should be noted that the recurring intensity drops could also be due to instability in the ion beam performance. The signal intensity of the barium and titanium are much higher than those of chromium, nickel, manganese and iron, which are almost at zero within the film region. Once the measurement reaches the film-substrate interface the barium and titanium signals decrease to zero while the alloying elements increase. This is also visualized in the EDS map (Fig. 5a, right) which shows two clearly separated regions with the substrate side of the interface having a strong chromium signal (colored red) and the film side being devoid of any chromium.

Upon heating to 750 °C, the elemental makeup remains mostly unchanged with the exception of the distribution of the chromium content (Fig. 5b). The depth profile shows that the chromium signal is reduced to

zero right at the film-substrate interface from its higher signal within the substrate before steadily increasing towards the film surface. This effect is observable through EDS as dark voids seen at the film-substrate interface, and highlighted in the right-hand side of Fig. 5b. Additionally, densification of the film is possibly observed as the disappearance of the recurring intensity drops in the barium and titanium signals and overall smoothing of their curves. Once again it should be noted that this might be an ion beam intensity issue, yet SEM micrographs measured from several different samples all appeared smooth and homogeneous after heat-treatment (Fig. 5b) and the accompanying voids seen in Fig. 5a disappeared as well.

### 4. Discussion

#### 4.1. Sintering origin

In this study, reproducible grain growth was observed in AD samples heat-treated at 750 °C. This result was expected due to the lowered BaTiO$_3$ sintering temperatures seen in thin-films compared to bulk materials [25]. The effect is often attributed to the usually nano-sized starting powders needed to make high quality thin films. Specifically, nanosized starting powders possess higher surface energy than powders consisting of larger grains in part due to their higher surface curvature which is proportional to the sintering rate [26].

AD films have characteristically small grains and sintering at lower temperatures is well reported in the literature at similar temperatures to the ones in the current study [27,28]. In particular, the amount of
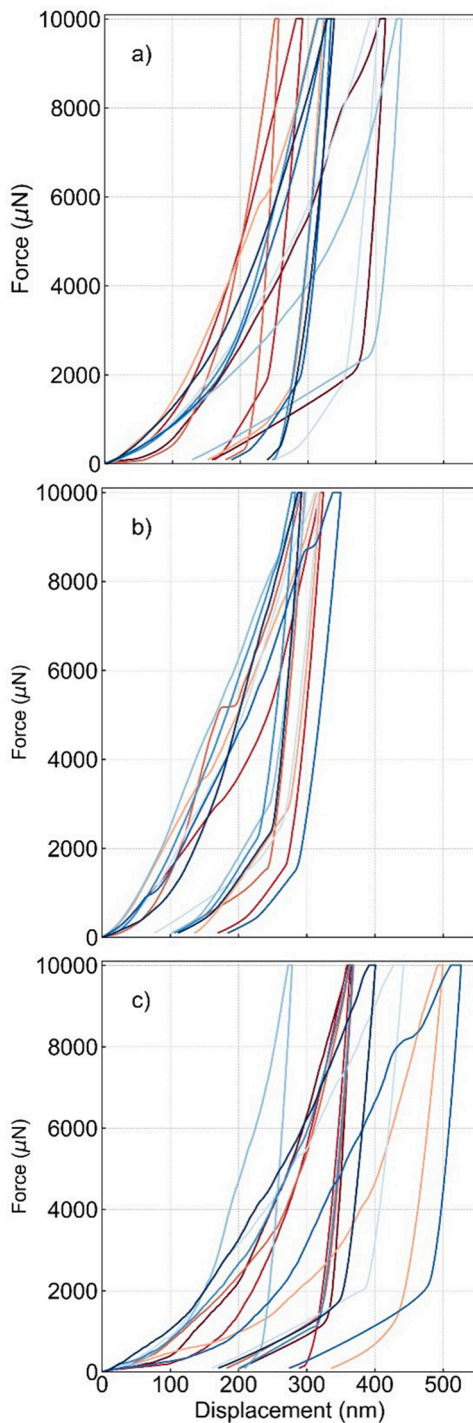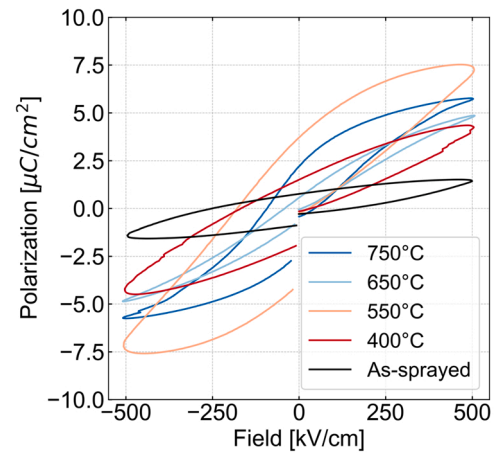
**Fig. 3.** Force-displacement curves of a) as-sprayed sample b) sample treated at 550 °C c) sample treated at 750 °C.

**Table 2**
Reduced modulus and hardness data for as-sprayed and heattreated samples.

| Condition | $E_r$ (GPa) | $H$ (GPa) |
|---|---|---|
| As-sprayed | $113.04 \pm 16.15$ | $2.62 \pm 0.73$ |
| 400°C | $118.48 \pm 16.49$ | $3.65 \pm 0.54$ |
| 550°C | $118.07 \pm 17.31$ | $3.43 \pm 0.42$ |
| 650°C | $101.76 \pm 32.97$ | $2.61 \pm 1.40$ |
| 750°C | $108.79 \pm 32.43$ | $2.14 \pm 0.78$ |



**Fig. 4.** Polarization-electric field loops for as-sprayed and heattreated AD samples.

crystallite growth reported for AD BaTiO$_3$ films after comparable heat-treatments are similar in the current study and the literature [27, 29]. However, SEM micrographs of AD film surfaces for comparable studies show surface grains in the size range of 100–200 nm [17,30]. The current study on the other hand reports exceptionally large surface grains ranging from $\sim$ 400 nm to $\sim$ 1.2 μm indicating the presence of an additional surface effect. One possible explanation could be the appearance of the chromium containing phase seen in Fig. 1a) which might be acting as a sintering aid.

The high chromium content observed at the surface of the films with exceptional grain-growth likely diffused there from the substrate. Based on Fig. 5b, both ToF- SIMS and EDS measurements show chromium depletion at the film-substrate interface visualized by the dark regions in the EDS. There is some evidence in the literature for this being the case as intergranular chromium precipitation occurs in austenite at 500 °C to 800 °C, resulting in depletion of chromium at the grain boundaries [31]. Furthermore, it has been suggested that this effect is caused by elevated chromium diffusion coefficients at grain boundaries relative to the bulk in stainless steel leading to depletion regions as the bulk diffusion is not fast enough to fill the chromium voids [32]. The elevated chromium diffusion at grain boundaries is particularly interesting when considering that AD films have high grain boundary densities on account of their powder-like microstructure. Such grain boundaries could provide favorable diffusion pathways towards the surface. Diffusion is possibly driven by chromium's high affinity for oxygen combined with the steep concentration gradient between the film's outer surface and the substrate. This type of diffusion would be analogous to the formation of Cr$_2$O$_3$ surface layers on stainless steel. In stainless steel, chromium metal will diffuse from the bulk to the surface due to chromium's affinity for oxygen in the air and oxidize. The resulting film is non-reactive and prevents further diffusion unless damaged, giving stainless steel its resistance to corrosion [33].

The presence of Cr towards the film's outer surface correlates with enhanced sintering behavior as seen in Fig. 2c. Furthermore, the magnitude of the grain growth correlated with film thickness (diffusion distance) in that thinner films showed more grain growth than thicker ones. SEM micrographs showing the correlation between film thickness and grain growth can be found in the supplementary materials. Multiple works have explored the efficacy of Cr$_2$O$_3$ as a sintering aid in Al$_2$O$_3$ and ZnO albeit with variable results [34–36]. Riu et al. [37] reported its efficacy in simultaneously enhancing grain growth and eliminating the presence of abnormal grains in Al$_2$O$_3$ when sintering at 1500 °C. This was attributed to chromium ions diffusing into the Al$_2$O$_3$ grains creating core-shell type structures in which coherency strain energy *i.e.* strain arising from changes to the molar volume as a function of composition at the grain boundary, enhanced the sintering rate [38]. Additionally, it
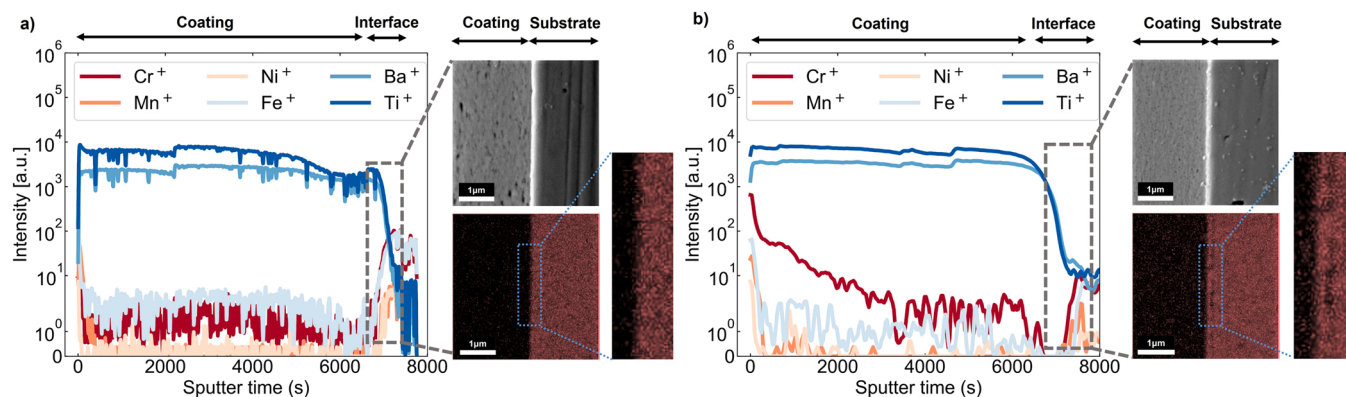
**Fig. 5.** Combined ToF-SIMS and EDS measurements for a) as-sprayed sample and b) sample heat-treated at 750 °C.

was noted by Riu et al. that chromium ion diffusion was several orders of magnitude higher at the surface than in the bulk also referring to earlier studies on chromium surface diffusion being elevated, especially at grain boundaries [39]. These findings support the hypothesis that chromium forms a grain boundary phase that enhances overall mass transport and supports grain growth analogous to the influence of transition metal oxide sintering aids [40].

*4.2. Dielectric properties*

Polarization behavior of the AD films was shown to improve with increasing heat-treatment temperatures. The lowest polarization values were observed in the as-sprayed samples. One of the characteristic effects observed in films produced by AD is the presence of large internal residual stresses introduced by the deposition mechanism [17,41], colloquially referred to as the "hammering effect". The hammering describes when an AD particle impacts with the substrate, leading to the fragmentation of the particle. The particle fragments dissipate their residual kinetic energy by rotating and reorienting at the surface and plastically deforming and rebinding with surrounding fragments [42]. This process repeats with every impact, resulting in successive compression of previously deposited fragments, leaving a substantial amount of residual internal stress. The unique microstructure of AD films which can be observed across different material systems are also attributed to this effect [7,12].

As residual internal stresses have been reported to alter the functional properties of certain ceramics [18] it is possible that the poor dielectric properties of the as-sprayed film are in part due to this stress. Additionally, the fragmentation of the particles during deposition produced crystallites which were ~ 9 nm, far smaller than the reported 1 μm − 2 μm grain size optimum for BaTiO$_3$ dielectric properties [16, 17]. Lastly, the as-sprayed samples were quite conductive which is another typical observation in otherwise insulating materials such as lead zirconium titanate (PZT) deposited by AD [10,43,44]. The reason for this increased conductivity in the as-sprayed samples is currently not well understood. However, it is suggested to be influenced by defect modulated space changes at the grain boundaries [13].

The release of residual internal stress was observed mainly in samples heat-treated at 400 °C and 550 °C as evident by clear shifts in the XRD spectra to higher angles (Fig. 1). Similar effects were observed by Khansur et al. [19] based on cross sectional stress distribution measurements using synchrotron x-ray microdiffraction which showed a decrease in compressive residual internal stress from − 672 MPa to − 271 MPa after annealing at 500 °C. In the present study, after the initial release at 550 °C, stress appears to have been reintroduced with heating to temperatures equal or higher than 650 °C. This can be seen in the XRD spectras shifting towards as-sprayed peak positions with increasing temperature. It is possibly due to this that the highest saturation polarization value is observed in samples heat-treated at 550 °C

(Fig. 4) and that it decreases at 650 °C albeit with added hysteresis behavior. Yet, this is difficult to determine due to the high conductivity of the samples. Despite an apparent increase in crystal strain for the 750 °C sample relative to the 650 °C one it had greatly enhanced saturation and remanent polarization values. This corresponds with a large increase in the grain sizes at the surface (Fig. 2c) as well as the highest crystallite sizes of any temperature condition (Table 1).

This gradual increase in polarization behavior with increasing crystallite size is consistent with the literature as seen in a study conducted by Hatono et al. [29]. Hatono's findings for crystallite growth in aerosol deposited BaTiO$_3$ on 304SUS stainless steel heat treated up to 800 °C were nearly identical to the calculated crystallite sizes in the current study (from an initial 10–20 nm at 800 °C) and resulted in a six-fold increase in the measured dielectric constant of the films.

Hoshina et al. proposed two relevant mechanisms behind the grain-size dependency of permittivity in BaTiO$_3$ nanoparticles and freestanding AD films [17,45]. The first mechanism suggests that sufficiently small BaTiO$_3$ nanoparticles at room temperature form core-shell structures consisting of a ferroelectric tetragonal core and a paraelectric cubic shell. These phases arise due to differences in lattice strain at the surface, resulting in a strain gradient towards the core. The cubic outer shell has been measured experimentally with a reported thickness of 10–15 nm regardless of particle size in the range of 20–1000 nm [45]. Because of this, the volume fraction of the cubic paraelectric phase becomes larger with decreasing grain size, negating ferroelectric behavior. Therefore, the mechanism predicts that a loss of ferroelectric character should occur for BaTiO$_3$ crystallites smaller than 20–30 nm as this would coincide with the complete disappearance of the tetragonal phase. Overall this mechanism appears to align well with the powder-like microstructure, high stress and low crystallite sizes of as-sprayed samples in this study, especially when considering the broad non-split seemingly psuedo-cubic appearence of XRD peaks observed in Fig. 1.

The second mechanism proposed by Hoshina was derived from work done on freestanding aerosol deposition BaTiO$_3$ films and focused on changes to the domain wall density [17]. Domain walls are widely reported as a contributing factor to piezo and ferroelectric properties [46–49] with the general effect being that increased domain wall densities result in enhanced ferroelectric properties. By looking at free standing films with grain sizes ranging from 170 to 24 nm it was found that relative permittivity decreased from 2800 to 670 with decreasing grain size [17]. It was suggested that this was due to the smaller grains being too small to possess more than one domain within its boundaries, leading to a loss of the multi-domain structure seen for larger grain sizes and a reduction in the total domain wall density for the material.

*4.3. Mechanical degradation*

Nanoindentation measurements highlight the existence of a cost-

benefit relationship between the mechanical and dielectric properties of the samples. As previously noted, the dielectric performance of the samples increase with increasing temperature (Fig. 4), yet the best dielectric performance coincides with a marked reduction in mechanical integrity. This is illustrated by the changes to the reduced modulus and hardness as well as the increase in measurement variability with changing temperature (Table 2), the origin of which can be seen in Fig. 3a-c.

Firstly, when looking at the force displacement curves for the as-sprayed sample one can see that the curves are slightly spaced out, indicating regions of different densities (Fig. 3a). Furthermore, most of the as-sprayed curves show a slightly exponential slope meaning that the AD film, which is akin to a compacted layer of powder, can initially be compressed. Lastly the presence of agglomerate-filled voids (Fig. 2b) can be seen as shoulders on some curves. At these points the indentor only has to exert a small amount of force to break up and displace the agglomerate within the void, leading to a momentary higher displacement relative to the force exerted.

These features of the curves are characteristic to the AD method when considering the RTIC mechanism. The powders used for the deposition had an initial $d_{50} \approx 1.2$ μm which can easily agglomerate within the aerosol generating unit [50]. These larger agglomerates do not undergo proper fracturing of its constituent particles upon impact with the substrate as their kinetic energy is released by breaking up the agglomerates rather than the particles themselves resulting in a poorly densified region or a void filled with larger particles [42,51]. Furthermore, as the fracture of impacting particles is affected by the hardness of the surface it collides with, the poorly densified regions left by the agglomerates can affect the density of several successive layers of the film [52].

Once heated to 550 °C, curve spacing has been significantly reduced, and the slopes are linear (Fig. 3b). The reduced spacing of the curves indicates an increase in the film homogeniety while the linear slopes are indicative of higher density. This is supported by the 550 °C sample possessing the second-highest $E_r$ and $H$ values of any sample (Table 2). The literature has previously suggested a link between the hardness of AD films and their dielectric performance. Kim et al. found that the dielectric performance of $BaTiO_3$ thin films deposited on stainless steel was significantly higher than films deposited on copper [52]. The authors suggested that this was due to weak particle-particle bonding, as well as highly rough film-substrate interfaces leading to higher leakage currents in samples deposited on copper. This is to be expected when considering the RTIC mechanism and the hardness of copper and stainless steel. Harder AD substrates result in more complete fracture of impacted particles during AD processing and gives denser, harder films with higher particle bonding [42]. On the other hand, softer substrates can be dented or partially penetrated by impacting particles, leading to rougher film-substrate interfaces [53]. As such, AD film hardness is linked to dielectric performance as it is a measure of densification and absence of pathways for leakage current to flow through. Consequently, the fact that the 550 °C treated samples in this study possessed the highest polarization values seems to be reflected by their high hardness and degree of densification relative to the as-sprayed samples. For temperatures higher than 550 °C the introduction of defects appears to have a significant effect on the film's mechanical properties. The 750 °C treated sample's force-displacement curves show increased spacing and large shoulders which are likely related to the presence of cracks. The presence of such defects corresponds to a reduction in mechanical properties (Table 2) and polarization values (Fig. 4) despite the fact that the samples had a high degree of densification (Fig. 2c)) which should have enhanced both [45,54].

The likely reason for this change is the introduction of cracks from sample expansion during heat-treatment reducing film cohesion, adhesion and creating paths for leakage current. A likely contributor to crack formation is the development of interfacial stresses between the film and substrate during heating. Such stresses were accurately described for AD films on yttrium stabilized zirconia, sapphire and silicon substrates by Han et al. [55] using a linear model for the total stress of $Pb_{1-x}Zr_xTiO_3$ thin films put forth by Desu et al. [56]. The model is a sum of the thermal, internal and extrinsic stresses during heating, where the thermal and extrinsic stresses are defined in Eqs. 1 and 2, respectively, and "internal stress" are the residual internal stresses caused by the AD process.

$$\sigma_{th} = \frac{E_f}{1 - v_f}(a_f - a_s)(T_d - T) \tag{1}$$

$$\sigma_{ex} = \frac{E_f}{1 - v_f}(\Delta V \big/ 3V) \tag{2}$$

Where $E_f$ is the elastic modulus of the film, $v_f$ is Poisson's ratio, $\alpha_f$ is the thermal expansion coefficient of the film, $\alpha_S$ is the thermal expansion coefficient of the substrate, while $T_d$ and $T$ are the heating and working temperature, respectively. Working temperature refers to the temperature at which subsequent testing is performed, which in the current study is 21 °C. Lastly $\Delta V/3V$ is the fractional volume change in the $BaTiO_3$ film as a result of its first order phase transition from tetragonal to cubic at the Curie temperature. If the total stress of a thin film exceeds the adhesion strength of the film to the substrate, or the strength of the particle- particle bonding within the film, cracks or delamination will occur. This makes AD films particularly hard to keep crack-free during heat-treatment due to the already high internal stresses from the deposition method which have been shown to increase with AD film thickness [13].

Considering Eq. 1, one can also see that the larger the thermal expansion coefficient mismatch the larger the interfacial stress contribution from the heat-treatment. In fact, this effect has been used specifically to make free-standing AD films by depositing them onto substrates with high thermal expansion coefficient mismatches to achieve delamination of intact films during heat-treatment [17]. However, for the purpose of well adhering, dense films this highlights an additional complication when considering post-deposition heat-treatments of AD samples as it further limits the choice of substrates to materials with similar thermal expansion coefficients.

In the current study, 304 stainless steel was used which has a similar thermal expansion coefficient to $BaTiO_3$ [57,58], as such the thermal expansion mismatch did not appear to become large enough at $T \leq 550$ °C to cause cracking as evident by the force displacement curves (Fig. 3). In fact, it appears that the substrate having only a slightly higher thermal expansion coefficient is beneficial during heat-treatments of $T \leq 550$ °C as it helps release some of the residual internal stress [19,55].

During heating the faster expansion of the substrate places the film under tensile stress. This counteracts some of the internal residual stress already present in the film which has been reported in the literature to be compressive [19,41]. Upon cooling the faster contraction of the substrate generates some compressive stress albeit depending on the maximum temperature this value might be lower than the initial residual internal stress leading to a net release.

This is possibly a contributor to the release of strain reported by Khansur et al. [19] and likely contributes to the enhancement of polarization behavior and the shifting of XRD peaks to higher angles (Fig. 1) in this study. However, for temperatures higher than 550 °C it appears that the internal residual stress has been adequately released and that any additional tensile stress serves to break particle-particle and film-substrate interface bonds. Such defects within the film are likely the main contributor to the high variance and shoulder formation seen in Fig. 3c. Furthermore, the XRD diffractograms of samples heat-treated at $T \geq 650$ °C show an increasingly large shift towards lower angles relative to samples treated at $T \leq 550$ °C indicating some reintroduction of compressive stress upon cooling (Fig. 1).

## 5. Conclusions

Thermal annealing of aerosol deposited $BaTiO_3$ up to 750 °C improves its dielectric properties. This enhancement likely stems from both a release of residual stress and significant grain growth. The appearance of grain growth coincides with diffusion of chromium from the substrate, suggesting that it acts as a sintering aid. For temperatures above 650 °C, mechanical degradation can be observed. The introduction of structural defects due to thermal expansion mismatch between the substrate and the aerosol film is discussed as the main mechanism determining the mechanical stability.

## Declaration of Competing Interest

The authors declare that they have no known competing financial interests or personal relationships that could have appeared to influence the work reported in this paper.

## Acknowledgments

## Appendix A. Supporting information

Supplementary data associated with this article can be found in the online version at doi:10.1016/j.jeurceramsoc.2023.03.012.

## References

[1] V.I. Mikla, V.V. Mikla, 7 ultrasound imaging. Medical Imaging Technology, Elsevier, Oxford, 2014, pp. 113–128, https://doi.org/10.1016/B978-0-12-417021-6.00007-1.

[2] J. Walker, T. Liu, M. Tendulkar, D.N. Burrows, C.T. DeRoo, R. Allured, E.N. Hertz, V. Cotroneo, P.B. Reid, E.D. Schwartz, T.N. Jackson, S. Trolier-McKinstry, Design and fabrication of prototype piezoelectric adjustable x-ray mirrors, Opt. Express 26 (21) (2018) 27757–27772.

[3] M. Saini, Y. Singh, P. Arora, V. Arora, K. Jain, Implant biomaterials: a comprehensive review, World J. Clin. Cases 3 (1) (2015) 52, https://doi.org/10.12998/wjcc.v3.i1.52.

[4] D.W. Hutmacher, J.T. Schantz, C.X.F. Lam, K.C. Tan, T.C. Lim, State of the art and future directions of scaffold-based bone engineering from a biomaterials perspective, J. Tissue Eng. Regen. Med. 1 (4) (2007) 245–260, https://doi.org/10.1002/term.24.

[5] B. McEntire, B. Bal, M. Rahaman, J. Chevalier, G. Pezzotti, Ceramics and ceramic coatings in orthopaedics, J. Eur. Ceram. Soc. 35 (16) (2015) 4327–4369, https://doi.org/10.1016/j.jeurceramsoc.2015.07.034.

[6] D. Hanft, J. Exner, M. Schubert, T. Stöcker, P. Fuierer, R. Moos, An overview of the aerosol deposition method: process fundamentals and new trends in materials applications, J. Ceram. Sci. Technol. 6 (2015) 147–182, https://doi.org/10.4416/JCST2015-00018.

[7] J. Exner, T. Nazarenus, D. Hanft, J. Kita, R. Moos, What happens during thermal post-treatment of powder aerosol deposited functional ceramic films? explanations based on an experiment-enhanced literature survey, Adv. Mater. 32 (19) (2020) 1908104, https://doi.org/10.1002/adma.201908104.

[8] M. Ichiki, J. Akedo, A. Schroth, R. Maeda, Y. Ishikawa, X-ray diffraction and scanning electron microscopy observation of lead zirconate titanate thick film formed by gas deposition method, Jpn. J. Appl. Phys. 36 (9S) (1997) 5815, https://doi.org/10.1143/jjap.36.5815.

[9] J. Akedo, M. Lebedev, Microstructure and electrical properties of lead zirconate titanate (Pb(Zr52/Ti48)O3) thick films deposited by aerosol deposition method, Jpn. J. Appl. Phys. 38 (9S) (1999) 5397, https://doi.org/10.1143/jjap.38.5397.

[10] J. Akedo, M. Lebedev, Effects of annealing and poling conditions on piezoelectric properties of Pb(Zr0.52Ti0.48)O3 thick films formed by aerosol deposition method, J. Cryst. Growth 235 (1–4) (2002) 415–420, https://doi.org/10.1016/s0022248(01)01925-x.

[11] J. Akedo, Aerosol deposition of ceramic thick films at room temperature: densification mechanism of ceramic layers, J. Am. Ceram. Soc. 89 (6) (2006) 1834–1839, https://doi.org/10.1111/j.1551-2916.2006.01030.x.

[12] J. Akedo, Room temperature impact consolidation (RTIC) of fine ceramic powder by aerosol deposition method and applications to microdevices, J. Therm. Spray. Technol. 17 (2) (2008) 181–198, https://doi.org/10.1007/s11666-008-9163-7.

[13] N.H. Khansur, U. Eckstein, L. Benker, U. Deisinger, B. Merle, K.G. Webber, Room temperature deposition of functional ceramic films on low-cost metal substrate, Ceram. Int. 44 (14) (2018) 16295–16301, https://doi.org/10.1016/j.ceramint.2018.06.027.

[14] C.-W. Kim, J.-H. Choi, H.-J. Kim, D.-W. Lee, C.-Y. Hyun, S.-M. Nam, Effects of interlayer roughness on deposition rate and morphology of aerosol-deposited Al2O3 thick films, Ceram. Int. 38 (7) (2012) 5621–5627, https://doi.org/10.1016/j.ceramint.2012.04.003.

[15] R. Sakamaki, T. Hoshina, H. Kakemoto, K. Yasuda, H. Takeda, J. Akedo, T. Tsurumi, Heat-cycle endurance and in-plane thermal expansion of Al2O3/Al substrates formed by aerosol deposition method, J. Ceram. Soc. Jpn. 116 (1360) (2008) 1299–1303, https://doi.org/10.2109/jcersj2.116.1299.

[16] D. Ghosh, A. Sakata, J. Carter, P.A. Thomas, H. Han, J.C. Nino, J.L. Jones, Domain wall displacement is the origin of superior permittivity and piezoelectricity in batio3 at intermediate grain sizes, Adv. Funct. Mater. 24 (7) (2014) 885–896, https://doi.org/10.1002/adfm.201301913.

[17] T. Hoshina, T. Furuta, Y. Kigoshi, S. Hatta, N. Horiuchi, H. Takeda, T. Tsurumi, Size effect of nanograined BaTiO 3 ceramics fabricated by aerosol deposition method, Jpn. J. Appl. Phys. 49 (9) (2010) 09MC02, https://doi.org/10.1143/jjap.49.09mc02.

[18] J. Ryu, J.-J. Choi, B.-D. Hahn, D.-S. Park, W.-H. Yoon, Ferroelectric and piezoelectric properties of 0.948 (K0.5Na0.5)NbO3−0.052 LiSbO3 lead-free piezoelectric thick film by aerosol deposition, Appl. Phys. Lett. 92 (1) (2008), 012905, https://doi.org/10.1063/1.2828892.

[19] N.H. Khansur, U. Eckstein, K. Riess, A. Martin, J. Drnec, U. Deisinger, K.G. Webber, Synchrotron x-ray microdiffraction study of residual stresses in BaTiO3 films deposited at room temperature by aerosol deposition, Scr. Mater. 157 (2018) 86–89, https://doi.org/10.1016/j.scriptamat.2018.07.045.

[20] M. Schubert, J. Exner, R. Moos, Influence of carrier gas composition on the stress of al2o3 coatings prepared by the aerosol deposition method, Materials 7 (8) (2014) 5633–5642, https://doi.org/10.3390/ma7085633.

[21] J. Adamczyk, P. Fuierer, Compressive stress in nanocrystalline titanium dioxide films by aerosol deposition, Surf. Coat. Technol. 350 (2018) 542–549, https://doi.org/10.1016/j.surfcoat.2018.07.015.

[22] M. Hasegawa, K. Kimura, K. Aoki, M. Komuro, Texture evolution of nickel coatings fabricated by aerosol deposition, Mater. Trans. 60 (11) (2019) 2305–2310, https://doi.org/10.2320/matertrans.MT-M2019161.

[23] Y. Kawakami, M. Watanabe, K.-I. Arai, S. Sugimoto, Piezoelectric properties and microstructure of BaTiO3 films on heatresistant stainless-steel substrates deposited using aerosol deposition, Trans. Mater. Res. Soc. Jpn. 41 (3) (2016) 279–283, https://doi.org/10.14723/tmrsj.41.279.

[24] Y. Imanaka, N. Hayashi, M. Takenouchi, J. Akedo, Aerosol deposition for post-LTCC, J. Eur. Ceram. Soc. 27 (8–9) (2007) 2789–2795, https://doi.org/10.1016/j.jeurceramsoc.2006.11.055.

[25] T. Yamamoto, T. Sakuma, Fabrication of barium titanate single crystals by solid-state grain growth, J. Am. Ceram. Soc. 77 (4) (1994) 1107–1109, https://doi.org/10.1111/j.11512916.1994.tb07281.x.

[26] D.W. Richerson, W.E. Lee, Modern Ceramic Engineering: Properties, Processing, and Use in Design, CRC Press is an imprint of the Taylor amp; Francis Group, an informa business, 2018.

[27] Z. Yao, C. Wang, Y. Li, H.-K. Kim, N.-Y. Kim, Effects of starting powder and thermal treatment on the aerosol deposited BaTiO3 thin films toward less leakage currents, Nanoscale Res. Lett. 9 (1) (2014) 435, https://doi.org/10.1186/1556-276x-9-435.

[28] D. Popovici, H. Tsuda, J. Akedo, Postdeposition annealing effect on (Ba0.6,Sr0.4) TiO3 thick films deposited by aerosol deposition method, J. Appl. Phys. 105 (6) (2009), 061638, https://doi.org/10.1063/1.3086197.

[29] H. Hatono, T. Ito, A. Matsumura, Application of BaTiO3 film deposited by aerosol deposition to decoupling capacitor, Jpn. J. Appl. Phys. 46 (10B) (2007) 6915–6919, https://doi.org/10.1143/jjap.46.6915.

[30] M. Suzuki, J. Akedo, Temperature dependence of dielectric properties of barium titanate ceramic films prepared by aerosol deposition method, Jpn. J. Appl. Phys. 49 (9) (2010) 09MA10, https://doi.org/10.1143/jjap.49.09ma10.

[31] S. Bruemmer, L. Charlot, Development of grain boundary chromium depletion in type 304 and 316 stainless steels, Scr. Metall. 20 (7) (1986) 1019–1024, https://doi.org/10.1016/0036-9748(86)90428-X.

[32] T. Thorvaldsson, A. Salwén, Measurement of diffusion coefficients for cr at low temperatures in a type 304 stainless steel, Scr. Metall. 18 (7) (1984) 739–742, https://doi.org/10.1016/0036-9748(84)90331-4.

[33] M. Navarro, A. Michiardi, O. Castaño, J. Planell, Biomaterials in orthopaedics, J. R. Soc. Interface 5 (27) (2008) 1137–1158, https://doi.org/10.1098/rsif.2008.0151.

[34] X. Xiao, L. Zheng, L. Cheng, T. Tian, X. Ruan, G. Li, Effect of Cr2O3 on the property and microstructure of ZnO–Bi2O3 varistor ceramics in different sintering temperature, Ceram. Int. 41 (2015) S557–S562, https://doi.org/10.1016/j.ceramint.2015.03.137.

[35] T. Parya, S. Banerjee, M. Sana, Densification of pure alpha alumina ceramics with chromia as dopant, J. Indian Chem. Soc. 89 (4) (2012) 533–541.

[36] D Szwagierczak, J Kulawik, A. Skwarek, Influence of processing on microstructure and electrical characteristics of multilayer varistors, cited By 14, J. Adv. Ceram. 8 (3) (2019) 408–417, https://doi.org/10.1007/s40145-019-0323-7.

[37] D.-H. Riu, Y.-M. Kong, H.-E. Kim, Effect of Cr2O3 addition on microstructural evolution and mechanical properties of Al2O3, J. Eur. Ceram. Soc. 20 (10) (2000) 1475–1481, https://doi.org/10.1016/s0955-2219(00)00023-6.

[38] Y.-K. Paek, H.-Y. Lee, S.-J.L. Kang, Direction of liquid film migration induced by chromic oxide in alumina-anorthite, J. Am. Ceram. Soc. 79 (12) (1996) 3029–3032, https://doi.org/10.1111/j.1151-2916.1996.tb08073.x.

[39] V.S. Stubican, G. Huzinec, D. Damjanovic, Diffusion of 51cr in surface layers of magnesia, alumina, and spinel, J. Am. Ceram. Soc. 68 (4) (1985) 181–184, https://doi.org/10.1111/j.1151-2916.1985.tb15294.x.

[40] M. Kodo, K. Soga, H. Yoshida, T. Yamamoto, Low temperature sintering of polycrystalline yttria by transition metal ion doping, J. Ceram. Soc. Jpn. 117 (1366) (2009) 765–768, https://doi.org/10.2109/jcersj2.117.765.

[41] M. Nakada, K. Ohashi, J. Akedo, Electro-optical properties and structures of (Pb, La)(Zr, Ti)O3 and PbTiO3 films prepared using aerosol deposition method, Jpn. J. Appl. Phys. 43 (9S) (2004) 6543, https://doi.org/10.1143/jjap.43.6543.

[42] J. Akedo, Room temperature impact consolidation and application to ceramic coatings: aerosol deposition method, J. Ceram. Soc. Jpn. 128 (3) (2020) 101–116, https://doi.org/10.2109/jcersj2.19196.

[43] G. Han, J. Ryu, W.-H. Yoon, J.-J. Choi, B.-D. Hahn, J.-W. Kim, D.-S. Park, C.-W. Ahn, S. Priya, D.-Y. Jeong, Stress-controlled Pb(Zr0.52Ti0.48)O3 thick films by thermal expansion mismatch between substrate and Pb(Zr0.52Ti0.48)O3 film, J. Appl. Phys. 110 (12) (2011), 124101, https://doi.org/10.1063/1.3669384.

[44] J.-J. Choi, B.-D. Hahn, J. Ryu, W.-H. Yoon, B.-K. Lee, D.-S. Park, Preparation and characterization of piezoelectric ceramic–polymer composite thick films by aerosol deposition for sensor application, Sens. Actuators A Phys. 153 (1) (2009) 89–95, https://doi.org/10.1016/j.sna.2009.04.025.

[45] T. Hoshina, S. Wada, Y. Kuroiwa, T. Tsurumi, Composite structure and size effect of barium titanate nanoparticles, Appl. Phys. Lett. 93 (19) (2008), 192914, https://doi.org/10.1063/1.3027067.

[46] T. Tsurumi, T. Sasaki, H. Kakemoto, T. Harigai, S. Wada, Domain contribution to direct and converse piezoelectric effects of PZT ceramics, Jpn. J. Appl. Phys. 43 (11A) (2004) 7618–7622, https://doi.org/10.1143/jjap.43.7618.

[47] A. Pramanick, D. Damjanovic, J.E. Daniels, J.C. Nino, J.L. Jones, Origins of electro-mechanical coupling in polycrystalline ferroelectrics during subcoercive electrical loading, J. Am. Ceram. Soc. 94 (2) (2011) 293–309, https://doi.org/10.1111/j.1551-2916.2010.04240.x.

[48] D. Damjanovic, M. Demartin, Contribution of the irreversible displacement of domain walls to the piezoelectric effect in barium titanate and lead zirconate titanate ceramics, J. Phys. Condens. Matter 9 (23) (1997) 4943–4953, https://doi.org/10.1088/0953-8984/9/23/018.

[49] N. Bassiri-Gharb, I. Fujii, E. Hong, S. Trolier-McKinstry, D.V. Taylor, D. Damjanovic, Domain wall contributions to the properties of piezoelectric thin films, J. Electroceram. 19 (1) (2007) 49–67, https://doi.org/10.1007/s10832-007-9001-1.

[50] K. Mihara, T. Hoshina, H. Takeda, T. Tsurumi, Controlling factors of film-thickness in improved aerosol deposition method, J. Ceram. Soc. Jpn. 117 (1368) (2009) 868–872, https://doi.org/10.2109/jcersj2.117.868.

[51] S.-M. Nam, N. Mori, H. Kakemoto, S. Wada, J. Akedo, T. Tsurumi, Alumina thick films as integral substrates using aerosol deposition method, Jpn. J. Appl. Phys. 43 (8A) (2004) 5414–5418, https://doi.org/10.1143/jjap.43.5414.

[52] H.-K. Kim, J.-M. Oh, S.I. Kim, H.-J. Kim, C.W. Lee, S.M. Nam, Relation between electrical properties of aerosoldeposited BaTiO3 thin films and their mechanical hardness measured by nano-indentation, Nanoscale Res. Lett. 7 (1) (2012) 264, https://doi.org/10.1186/1556-276x-7-264.

[53] T. Schmidt, H. Assadi, F. Gärtner, H. Richter, T. Stoltenhoff, H. Kreye, T. Klassen, From particle acceleration to impact and bonding in cold spraying, J. Therm. Spray. Technol. 18 (5–6) (2009) 794, https://doi.org/10.1007/s11666-009-9357-7.

[54] V. Buscaglia, C.A. Randall, Size and scaling effects in barium titanate. An overview, J. Eur. Ceram. Soc. 40 (11) (2020) 3744–3758, https://doi.org/10.1016/j.jeurceramsoc.2020.01.021.

[55] G. Han, J. Ryu, W.-H. Yoon, J.-J. Choi, B.-D. Hahn, J.-W. Kim, D.-S. Park, C.-W. Ahn, S. Priya, D.-Y. Jeong, Stress-controlled Pb(Zr0.52Ti0.48)O3 thick films by thermal expansion mismatch between substrate and Pb(Zr0.52Ti0.48)O3 film, J. Appl. Phys. 110 (12) (2011), 124101, https://doi.org/10.1063/1.3669384.

[56] S.B. Desu, Influence of stresses on the properties of ferroelectric BaTiO3 thin films, J. Electrochem. Soc. 140 (10) (1993) 2981–2987, https://doi.org/10.1149/1.2220943.

[57] J.A. Bland, The thermal expansion of cubic barium titanate (batio3) from 350°c to 1050°c, Can. J. Phys. 37 (4) (1959) 417–421, https://doi.org/10.1139/p59-046.

[58] T. Sasaki, K. Watanabe, K. Nohara, Y. Ono, N. Kondo, S. Sato, Physical and mechanical properties of high manganese non-magnetic steel and its application to various products for commercial use, Trans. Iron Steel Inst. Jpn. 22 (12) (1982) 1010–1020, https://doi.org/10.2355/isijinternational1966.22.1010.